Supporting Information

Magnetic and structural transitions tuned through valence electron concentration in magnetocaloric $Mn(Co_{1-x}Ni_x)Ge$

Qingyong Ren,*[,†,§,#,‖] Wayne D. Hutchison,*[,†] Jianli Wang,*[,‡,¶] Andrew J. Studer,[⊥] and Stewart J. Campbell[†]

[†]School of Physical, Environmental and Mathematical Sciences, The University of New South Wales, Canberra at the Australian Defence Force Academy, Canberra, Australian Capital Territory 2600, Australia
[‡]Institute for Superconductivity and Electronic Materials, University of Wollongong, Wollongong, New South Wales 2500, Australia
[⊥]Australian Centre for Neutron Scattering, Locked Bag 2001, Kirrawee DC NSW 2232, Australia
[§]School of Physics and Astronomy and [#]Key Laboratory of Artificial Structures and Quantum Control, School of Physics and Astronomy, Shanghai Jiao Tong University, Shanghai, 200240, China
[‖]Collaborative Innovation Center for Advanced Microstructures, Nanjing 210093, China
[¶]College of Physics, Jilin University, Changchun 130012, China

Table of Contents

1 Crystallographic tructures

1.1 Atomic networks

In the orthorhombic structure (*Pnma*) of MnCoGe/MnNiGe-based compounds, each Mn atom has four Mn nearest-neighbors with two characteristic Mn-Mn separations, d_1 and d_2, as shown in Figure S1. The Mn atoms form 3 dimensional (3D) Mn-Mn interaction networks. This 3D Mn-Mn network comprises of two zigzag chains which penetrate through two groups of Co/Ni-Ge rings along the a_{orth}-axis (corresponding to d_1) and the b_{orth}-axis.

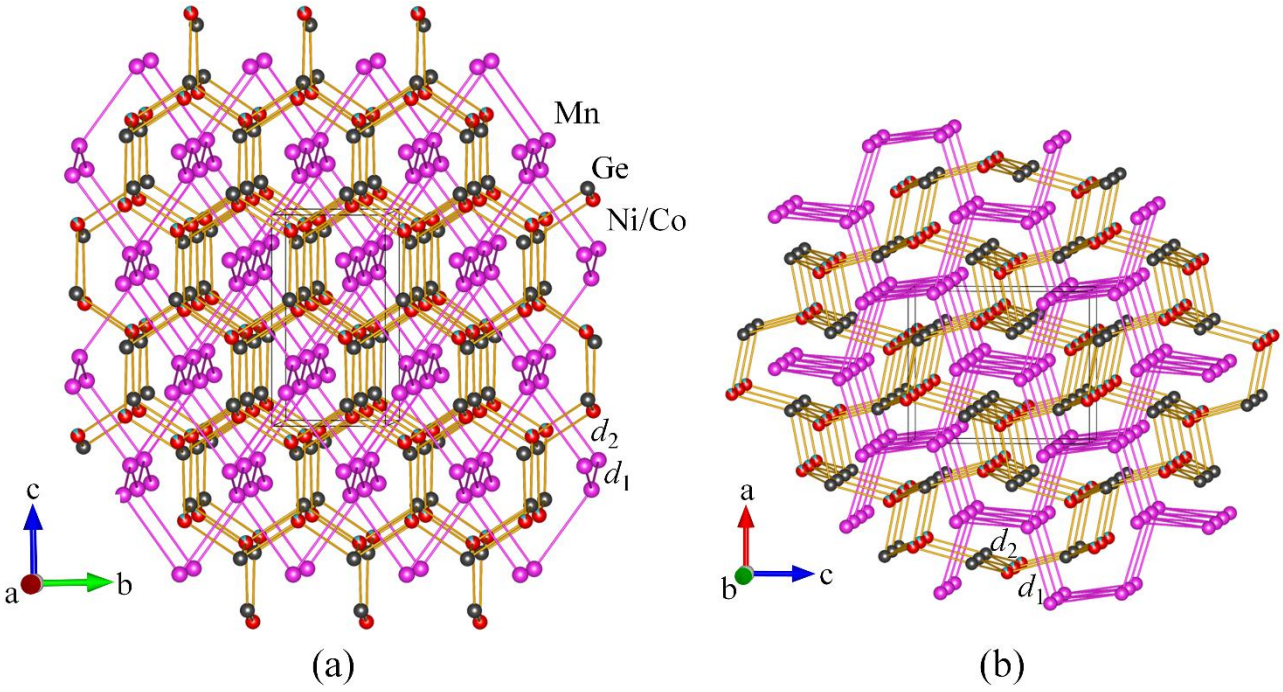

Figure S1 Mn-Mn networks in the Co/Ni-Ge networks in the orthorhombic phase of the $Mn(Co_{0.86}Ni_{0.14})Ge$ sample. (Lattice parameters and atomic positions are from the Rietveld refinement of the neutron pattern at 5 K, see Figure S4(a)). In the Co/Ni-Ge networks, there are two tunnels: (a) along the a_{orth}-axis built up from the honeycomb, and (b) along the b_{orth}-axis through the eight-rings which form from the partial break of Ni/Co-Ge bonds between the Co/Ni-Ge layers during the martensitic transition. There are two kinds of Mn-Mn nearest neighbors, d_1 and d_2, penetrating these two kinds of tunnels.

1.2 Analysis of x-ray diffraction patterns

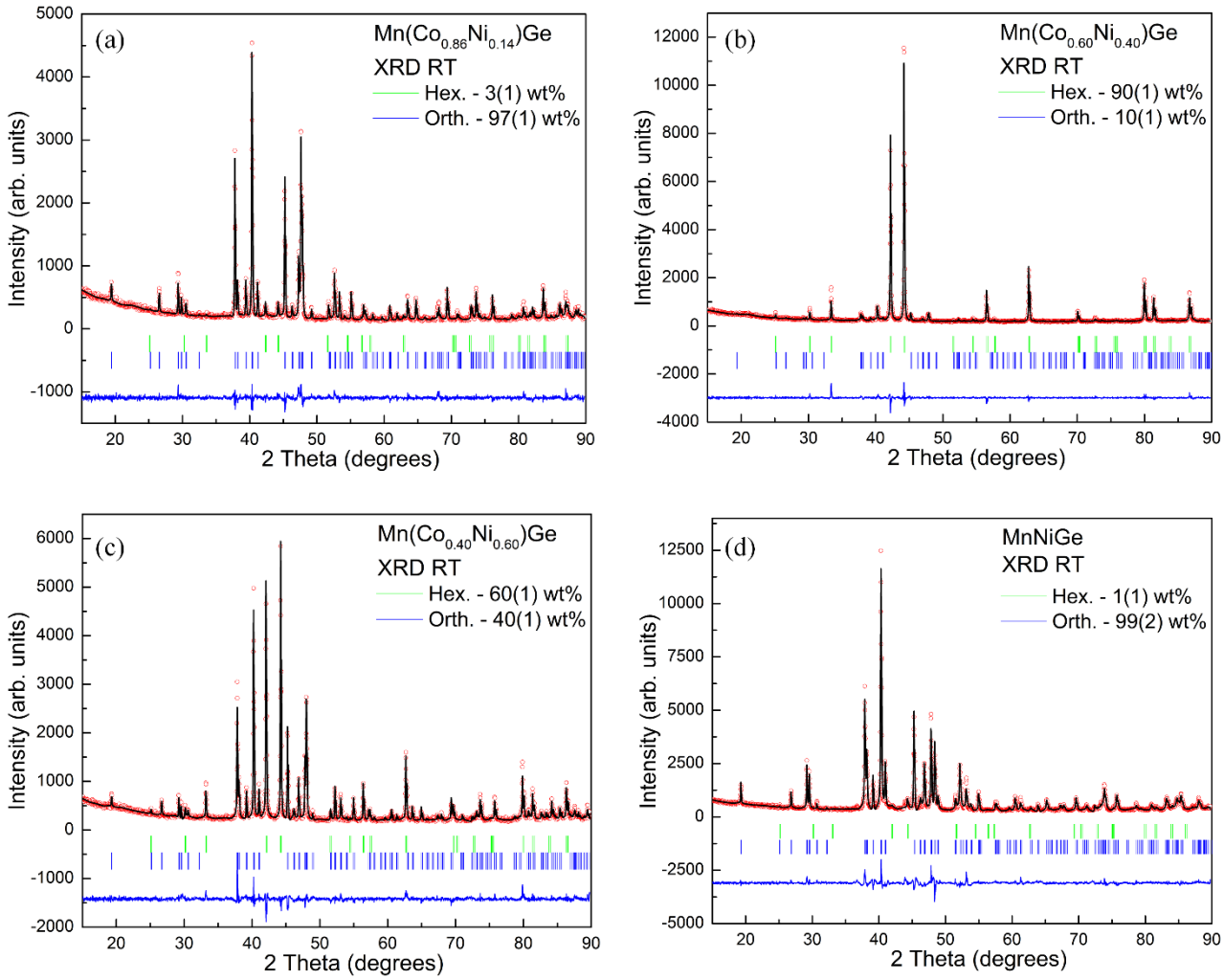

Figure S2 Rietveld refinements of the x-ray diffraction patterns for (a) $Mn(Co_{0.86}Ni_{0.14})Ge$, (b) $Mn(Co_{0.60}Ni_{0.40})$, (c) $Mn(Co_{0.40}Ni_{0.60})Ge$ and (d) MnNiGe at room temperature. The circles and solid lines on the circles are observed and calculated data, respectively. The horizontal rows of Bragg markers (from top to bottom) represent structures of the hexagonal and the orthorhombic phases, respectively. The trace lines represent the difference between observed and calculated data. Fractions of the hexagonal and the orthorhombic phases are given. No impurity phase was observed in these diffraction patterns. It is noted that the neutron diffraction experiments demonstrate a tiny impurity phase in the $Mn(Co_{1-x}Ni_x)Ge$ samples with x = 0.90 and 1.00. It is $MnCo_{1.25}Ge_{0.75}$ with a space group of *P6₃/mmc*. The phase fraction of this impurity is so small (≤ 2(1) wt%) that the x-ray diffraction experiment cannot identify.

As shown in Figure 3 in the main context, the variation of lattice parameters of the orthorhombic phase agrees well with the Vegard's law in Mn(Co1-xNix)Ge in the region of x = 0.12, 0.14, …, 0.20,

far below the critical concentration for the occurrence of spiral magnetic structures (x = ~0.55). This observation confirms the slight increase in the Ni concentration, confirming the correctness of our careful sample preparation procedures.

2 Magnetization

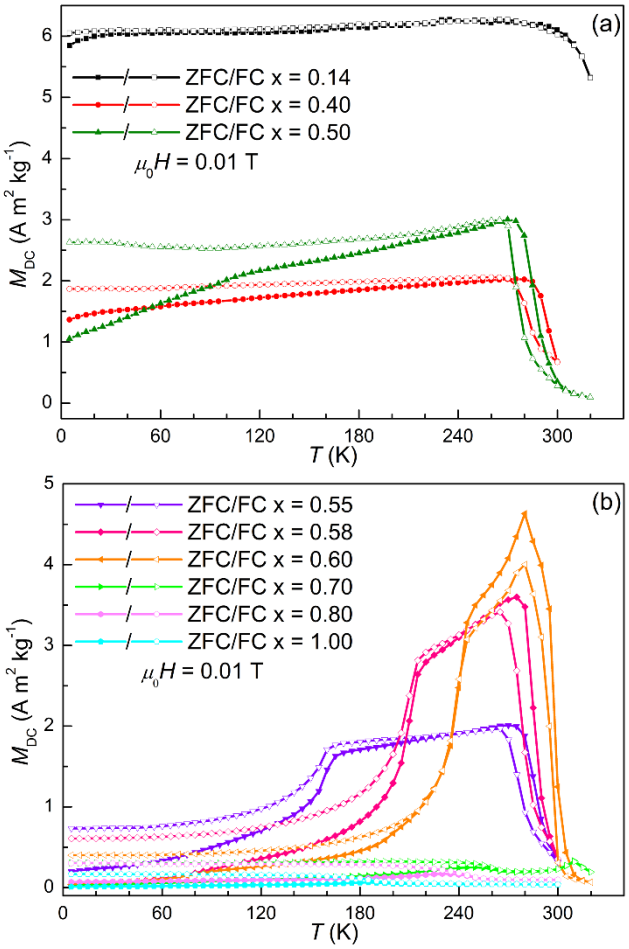

Figure S3 Magnetization curves as a function of temperature for the $Mn(Co_{1-x}Ni_x)Ge$ samples, (1) x = 0.20, 0.40, 0.50 and (b) x = 0.55, 0.58, 0.60, 0.70, 0.80 and 1.00, in an applied field of 0.01 T on warming after zero-field cooling (ZFC, solid symbols) and field cooling (FC, open symbols).

3 Phase transition temperatures

Table S1 Phase transition temperatures for annealed $Mn(Co_{1-x}Ni_x)Ge$ as determined from variable temperature x-ray diffraction and neutron diffraction experiments, and magnetization measurements.

x	T_M* (K)	FWHM (K)	$T_m^{W‡}$ (K)	$T_m^{C‡}$ (K)	T_C (K)	T_N or T_N^{SP-FM} (K)
0.14	370(2)	38(2)	-	-	345(5)	-
0.30	324(5)	-	-	-	-	-
0.40	299(1)	13(1)	295(4)	280(4)	-	-
0.50	290(1)	17(1)	285(4)	275(4)	-	-
0.55	291(1)	14(1)	285(4)	275(4)	-	155(4)/170(5)†
0.58	290(1)	18(1)	285(4)	280(4)	-	210(4)/215(5)
0.60	312(1)	15(1)	300(4)	295(4)	-	240(4)/245(5)
0.70	-	-	-	-	-	306(5)
0.90	442(5)	20(5)	-	-	-	350(5)
1.00	-	-	-	-	-	360(5)

* The structural transition temperature T_M for x = 0.30, 0.50 and 0.55 are estimated from variable temperature x-ray diffraction experiments, with the other data derived from the neutron powder diffraction experiments.

‡ To distinguish the magnetic transitions around a magneto-structural transition and around a Curie temperature, the magnetization change temperatures are marked using T_m^W and T_m^C around the magneto-structural transition.

† Magnetic transitions temperatures T_N^{SP-FM} derived from magnetization and neutron diffraction experiments, respectively.

4 Analysis of neutron diffraction patterns

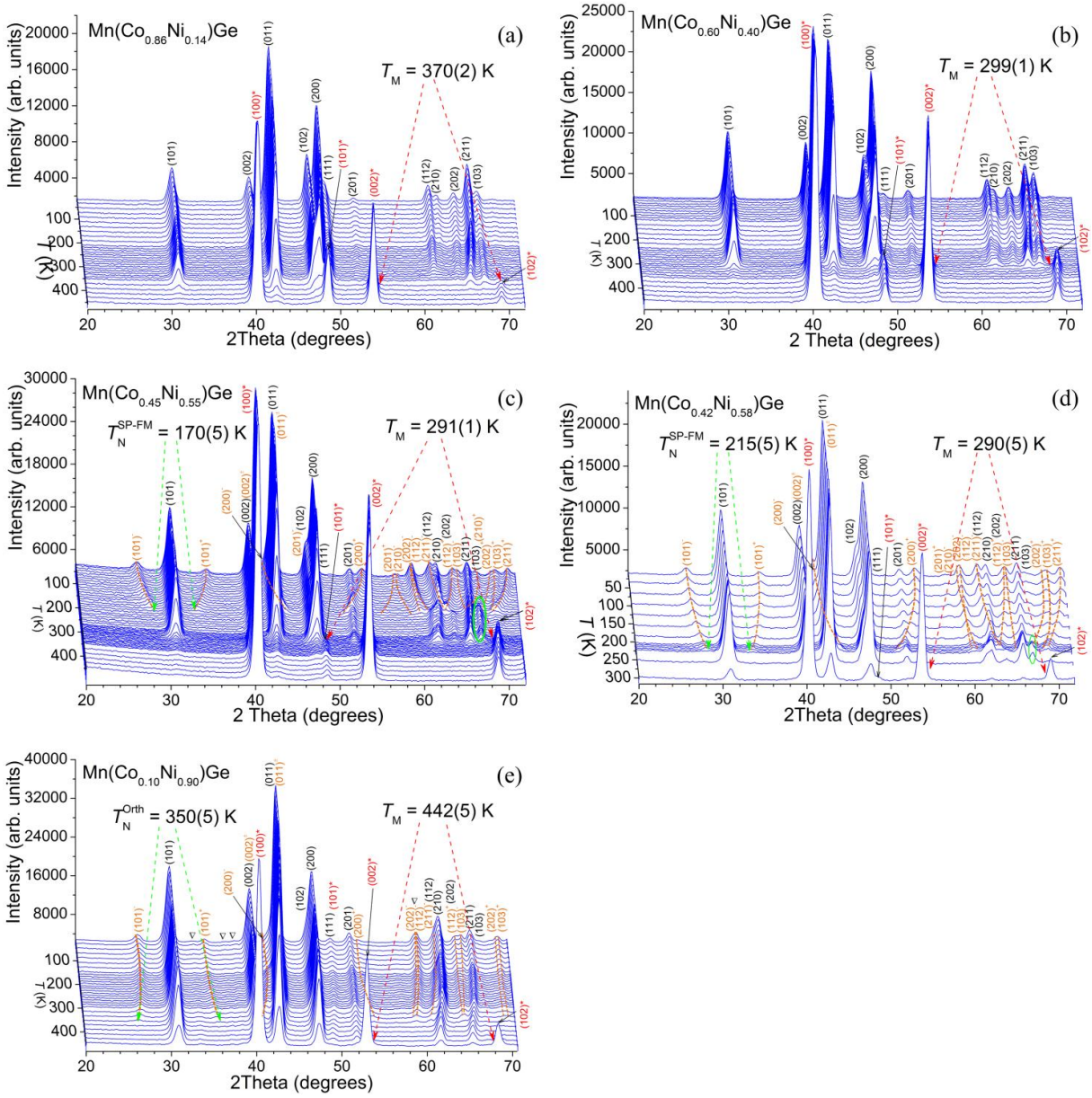

Figure S4 Powder neutron diffraction patterns (λ = 2.4143 Å) over the temperature range 10 K to 450 K for $Mn(Co_{1-x}Ni_x)Ge$ with (a) x = 0.14, (b) x = 0.40, (c) x = 0.55, (d) x = 0.58 and (e) x = 0.90. (The diffraction patterns for x = 0.60 and x = 1.00 are shown in Figs. 5(a) and 5(d).) All of the peaks are identified as the orthorhombic (Miller indices without asterisk) and hexagonal (Miller indices with asterisks) structures in the samples with x = 0.14, 0.40, 0.55 and 0.58. In the sample with x = 0.90, the impurity phase $MnNi_{1.25}Ge_{0.75}$ (*$P6_3/mmc$*, indicated by triangles) is also observed. The curves in (c), (d) and (e) are guides for the evolution of the magnetic satellite peaks. Some satellite peaks which are too small to be discerned are not marked. T_M, T_N^{SP-FM} and T_N^{Orth} are the temperatures for the reverse martensitic transformation, spiral-AFM/FM transition in the orthorhombic structure and the AFM/FM transition in the orthorhombic structure.

4.1 Atomic occupancies

Table S2 The nominal compositions and the actual compositions which are determined from the Rietveld refinements of the neutron diffraction patterns. No mixing atomic distribution was observed between Mn and Ni.

Nominal Composition	Neutron Diffraction-Composition
$Mn(Co_{0.86}Ni_{0.14})Ge$	$Mn(Co_{0.864}Ni_{0.136})Ge$
$Mn(Co_{0.60}Ni_{0.40})Ge$	$Mn(Co_{0.612}Ni_{0.388})Ge$
$Mn(Co_{0.45}Ni_{0.55})Ge$	$Mn(Co_{0.428}Ni_{0.572})Ge$
$Mn(Co_{0.42}Ni_{0.58})Ge$	$Mn(Co_{0.416}Ni_{0.584})Ge$
$Mn(Co_{0.40}Ni_{0.60})Ge$	$Mn(Co_{0.382}Ni_{0.618})Ge$
$Mn(Co_{0.10}Ni_{0.90})Ge$	$Mn(Co_{0.102}Ni_{0.898})Ge$
MnNiGe	$MnNi_{0.996}Ge$

4.2 Irreducible representation analysis of ferromagnetic structures

The magnetization data for $Mn(Co_{0.86}Ni_{0.14})Ge$ and $Mn(Co_{0.60}Ni_{0.40})Ge$ (Figure 4(a)) shows features that suggest ferromagnetism. It is straightforward to analyze the ferromagnetic structure using irreducible representations. Therefore, irreducible representation analyses were carried out for both samples using BasIreps program in FullProf suite. For the 4c site (Mn atoms occupy 4c sites) in the orthorhombic structure (*Pnma*), the decomposition of the magnetic representation comprises eight representations:

$$\Gamma_{\mathrm{Mag}}^{4c} = 1\Gamma_1 + 2\Gamma_2 + 2\Gamma_3 + 1\Gamma_4 + 1\Gamma_5 + 2\Gamma_6 + 2\Gamma_7 + 1\Gamma_8. \quad (S.1)$$

The basis vectors of these irreducible representations are given in Table S2.

Table S3 Irreducible representation analysis for the 4c site in the orthorhombic structure (*Pnma*) with a propagation vector [0 0 0]. The atomic position for the 4c site are (x, ¼, y), (½ – x, ¾, ½ + z), (-x, ¾, -z), and (½ + x, ¼, -z).

Representation	Ordering mode	Magnetic moment directions		
		x	y	z
Γ_1	G_y		+ - + -	
Γ_2	A_xC_z	+ - - +		+ + - -
Γ_3	G_xF_z	+ - + -		+ + + +
Γ_4	A_y		+ - - +	
Γ_5	F_y		+ + + +	
Γ_6	C_xA_z	+ + - -		+ - - +
Γ_7	F_xG_z	+ + + +		+ - + -
Γ_8	C_y		+ + - -	

All of these representation models were simulated and a comparison of these simulations with the neutron diffraction patterns indicated that F_z of Γ_3 and F_y of Γ_5, corresponding to a ferromagnetic structure along the c_{orth}-axis and b_{orth}-axis, are the best models for $Mn(Co_{0.86}Ni_{0.14})Ge$ and $Mn(Co_{0.60}Ni_{0.40})Ge$, respectively. Figures S5(a) and S5(b) are the Rietveld refinements of the neutron diffraction patterns using the models F_z of Γ_3 and F_y of Γ_5 for $Mn(Co_{0.86}Ni_{0.14})Ge$ and $Mn(Co_{0.60}Ni_{0.40})Ge$, respectively, at 5 K. Three phases were considered in the refinements corresponding to: the nuclear and magnetic scattering from the orthorhombic phase and the nuclear

scattering of the hexagonal phase. (For comparison, the Rietveld refinement using F_z of Γ_3 for $Mn(Co_{0.60}Ni_{0.40})Ge$ gives bad fitting as shown in Figure S5(c)).

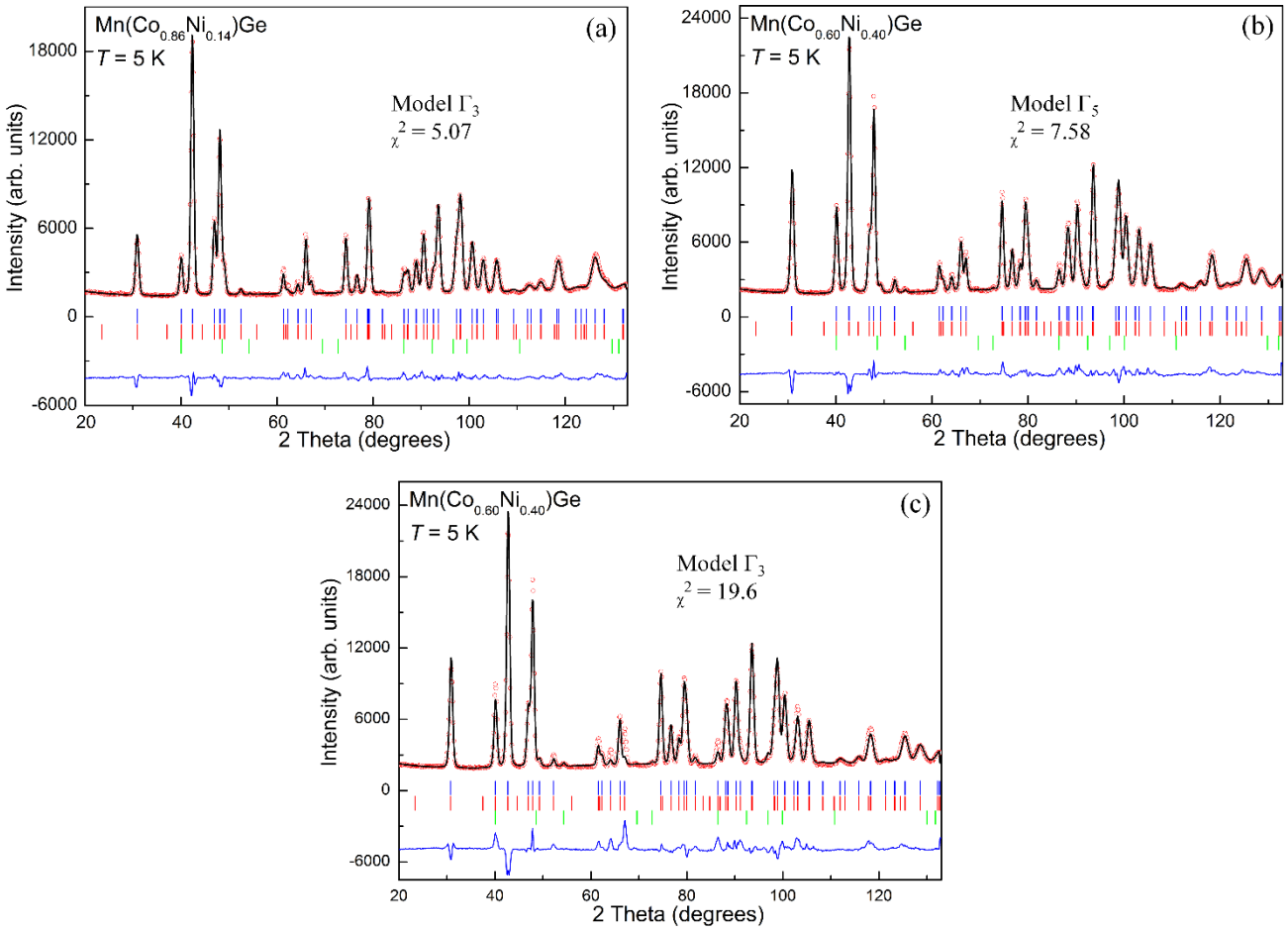

Figure S5 Rietveld refinements of the neutron diffraction patterns for (a) $Mn(Co_{0.86}Ni_{0.14})Ge$ using model F_z of Γ_3, (b) $Mn(Co_{0.60}Ni_{0.40})Ge$ using model F_y of Γ_5 and (c) $Mn(Co_{0.60}Ni_{0.40})Ge$ using model F_z of Γ_3 at 5 K. The circles and solid lines on the circles are observed and calculated data, respectively. The horizontal rows of Bragg markers (from top to bottom) represent the nuclear and magnetic structures of orthorhombic, and the nuclear structure of the hexagonal phase, respectively. The trace lines represent the difference between observed and calculated data. F_z of Γ_3 and F_y of Γ_5 are the best models for $Mn(Co_{0.86}Ni_{0.14})Ge$ and $Mn(Co_{0.60}Ni_{0.40})Ge$, respectively. Compared with the refinement based on model F_y of Γ_5 as shown in (b), F_z of Γ_3 gives a poor quality fitting for $Mn(Co_{0.60}Ni_{0.40})Ge$ (see (c)).

4.3 AFM/FM transitions in the samples with x = 0.55 to 0.60

As shown in Figs. 7(a), S2(c) and S2(d), there is a AFM/FM transition at 175(5) K, 215(5) K and 245(5) K in $Mn(Co_{0.45}Ni_{0.55})Ge$, $Mn(Co_{0.42}Ni_{0.58})Ge$ and $Mn(Co_{0.40}Ni_{0.60})Ge$, respectively. This magnetic transition is accompanied by the disappearance of the satellite peaks and the enhancements of some nuclear scattering peaks, such as the $(101)_{orth}$ and $(103)_{orth}$ peaks. The thermal evolution of the $(101)_{orth}$ peak intensity for $Mn(Co_{0.45}Ni_{0.55})Ge$ and $Mn(Co_{0.40}Ni_{0.60})Ge$ are shown in Figure S3. Abrupt enhancement is observed in both samples. Following analysis of neutron patterns indicate that the ferromagnetic (FM) structure is similar to that in $Mn(Co_{0.60}Ni_{0.40})Ge$ with magnetic moments pointing to the b_{orth}-axis.

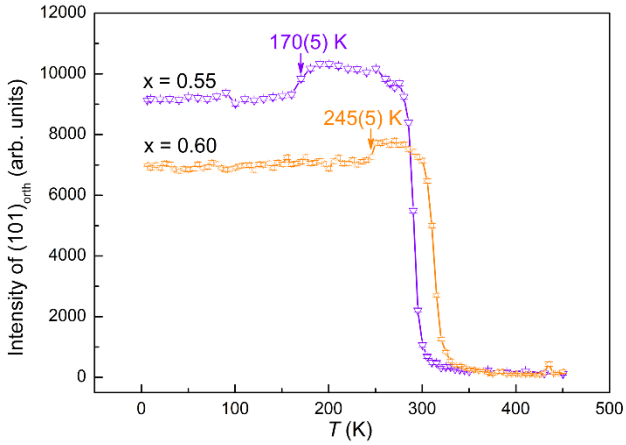

Figure S6 Thermal variation of the $(101)_{orth}$ peak intensity for $Mn(Co_{0.45}Ni_{0.55})Ge$ and $Mn(Co_{0.40}Ni_{0.60})Ge$. The $(101)_{orth}$ peak intensity is found to increase sharply in both the $Mn(Co_{0.45}Ni_{0.55})Ge$ and $Mn(Co_{0.40}Ni_{0.60})Ge$ samples at 175(5) K and 245(5) K, respectively.

4.4 Analysis of incommensurate magnetic structures

For the $Mn(Co_{1-x}Ni_x)Ge$ samples, there are spiral magnetic structures in the incommensurate region. The FullProf suite can be used to describe a spiral structure. In this work, the conical magnetic model (jbt = 5) were used. (jbt: structure factor model and refinement method for the phase).

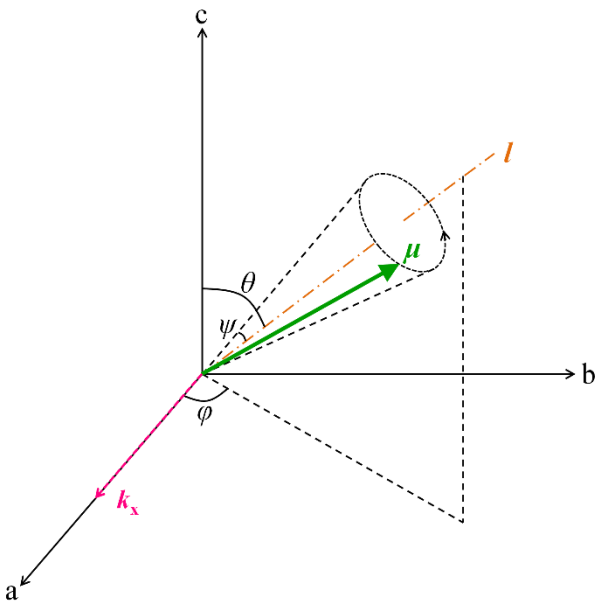

Figure S7 Coordinate system for a conical magnetic structure used in the Rietveld refinement based on FullProf suite. The spin vector $\boldsymbol{\mu}$ lies on the cone with a half-angle ψ. θ and φ are the spherical angles of the cone axis (spiral axis) $\boldsymbol{l}$ of the first atom with respect to the coordinate system.

4.4.1 Determination of spherical angles

Variation of the parameters ψ, θ and φ in the spiral structures produce only small differences in the magnetic diffraction patterns. This makes the refinement of these angles difficult. To search for the best refinement, different angles were tried (in 10° steps per refinement). As an example, parameters from refinements using different values of angle θ are shown in Figure S7. The best refinement with the smallest reduced chi-square is 70° (or 110°) for the $Mn(Co_{0.40}Ni_{0.60})Ge$ sample at 5 K.

In the $Mn(Co_{1-x}Ni_x)Ge$ samples, the incommensurate magnetic structures have ψ = 90° (flat spiral-structure) and φ = 0°. θ varies between 0° and 90° in the *ac*-plane with Ni content x and temperature (see Figure S8). For examples, θ = 70°, 0° and 90° - corresponding to: a cycloidal-spiral structure, a simple cycloidal structure in the *bc*-plane and a simple spiral structure in the *ab*-plane for $Mn(Co_{0.40}Ni_{0.60})Ge$ (5 K, see Figure 6(c)), MnNiGe (5 K, see Figure 6(d)) and $Mn(Co_{0.10}Ni_{0.90})Ge$ (at 180 K, see Figure S9), respectively.

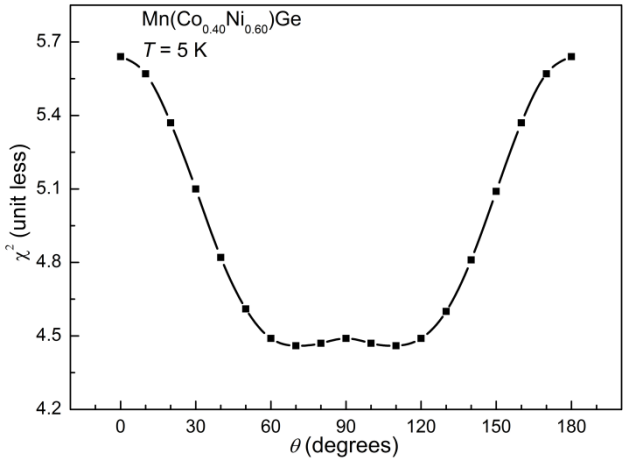

Figure S8 Reduced chi-square χ^2 of the refinement results as a function of the cone axis angle θ for the neutron powder diffraction pattern of $Mn(Co_{0.40}Ni_{0.60})Ge$ at 5 K.

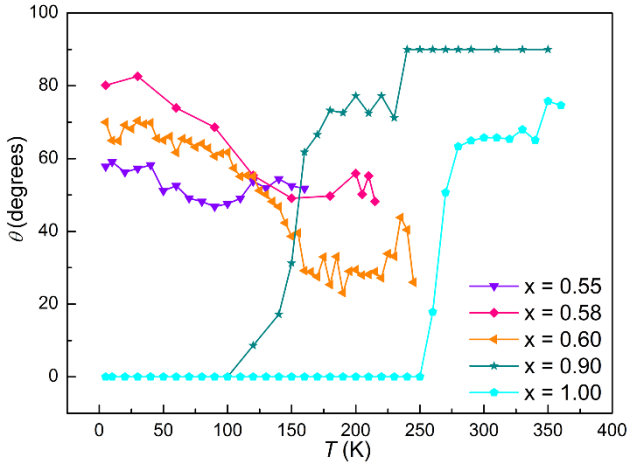

Figure S9 The angles θ of the spiral axis ***l*** as functions of temperature for the spiral structure in the orthorhombic structure of the $Mn(Co_{1-x}Ni_x)Ge$ samples (x = 0.55 to 1.00). Note: ***l*** varies in the *ac*-plane.

4.4.2 Rietveld refinements of different spiral structures

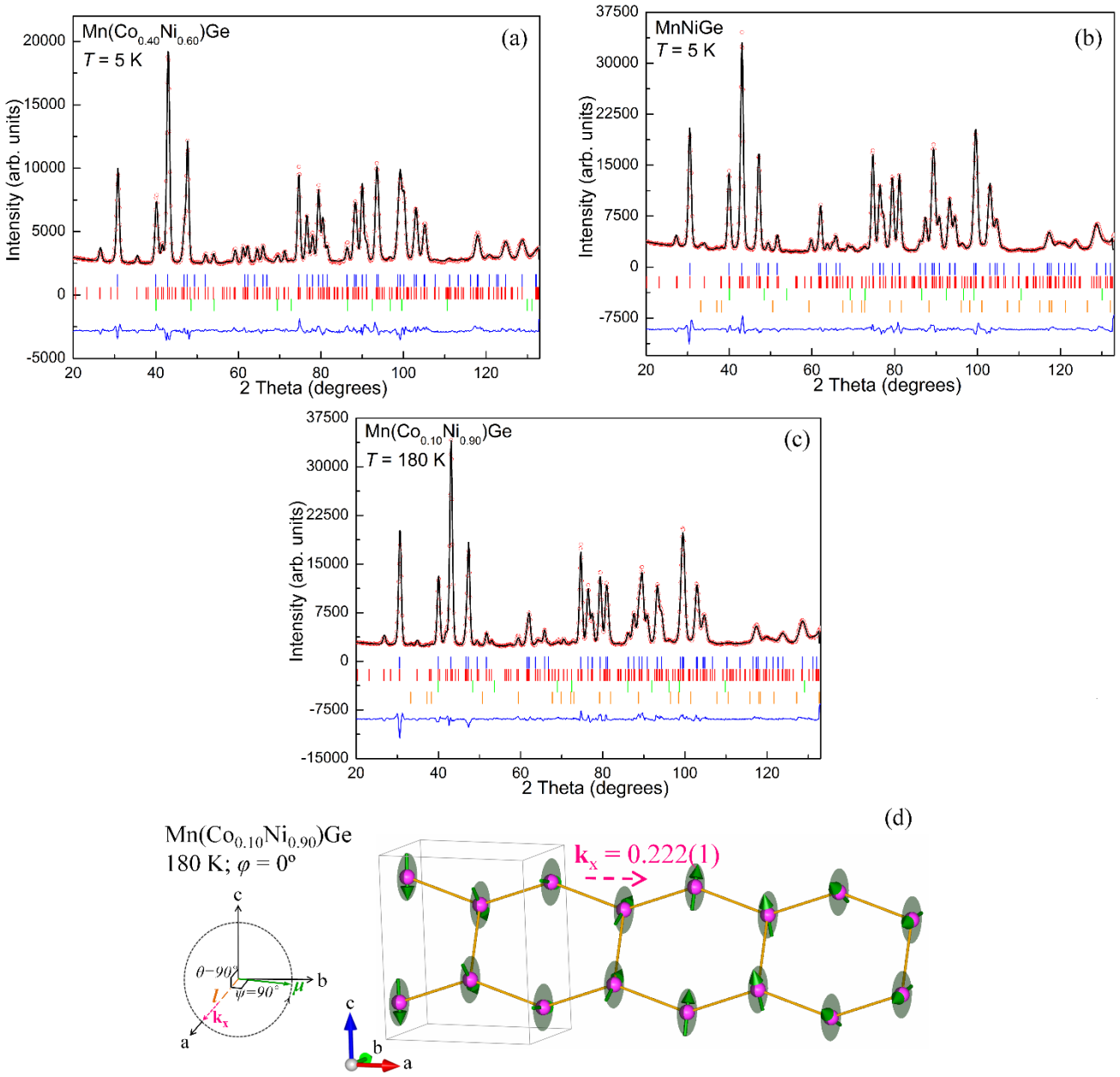

Figure S10 (a) Rietveld refinements of the neutron diffraction patterns for (a) $Mn(Co_{0.40}Ni_{0.60})Ge$ at 5 K, (b) MnNiGe at 5 K and (c) $Mn(Co_{0.10}Ni_{0.90})Ge$ at 180 K. The circles and solid lines on the circles are observed and calculated data, respectively. The horizontal rows of Bragg markers (from top to bottom) represent the nuclear and magnetic structures of the orthorhombic phase, the nuclear structures of the hexagonal phase and the $MnNi_{1.25}Ge_{0.75}$ impurity, respectively. The bottom lines are the difference between observed and calculated data. (d) is the magnetic structure of the orthorhombic phase for $Mn(Co_{0.10}Ni_{0.90})Ge$ at 180 K. The propagation vector is 0.222(1) along a_{orth}. The magnetic structures for $Mn(Co_{0.40}Ni_{0.60})Ge$ and MnNiGe at 5 K are given in Figures 6(b) and 6(d), respectively.

4.5 Magnetic moments

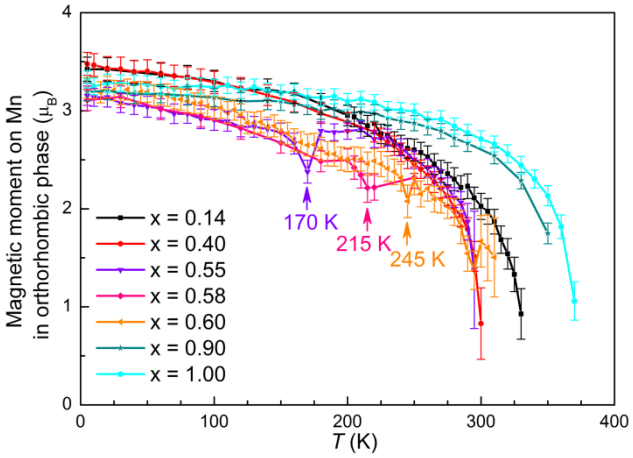

Figure S11 The variation of the magnetic moments with temperature for the Mn sublattice in the orthorhombic structure of $Mn(Co_{1-x}Ni_x)Ge$. The three dips noted around ~170 K, ~215 K and ~245 K, for the $Mn(Co_{1-x}Ni_x)Ge$ samples with x = 0.55, 0.58 and 0.60 may originate from difficulties with models used for the Rietveld refinement of the mixed spiral-AFM and FM_b.

5 Magnetic interactions

5.1 Thermal evolution of lattice parameters

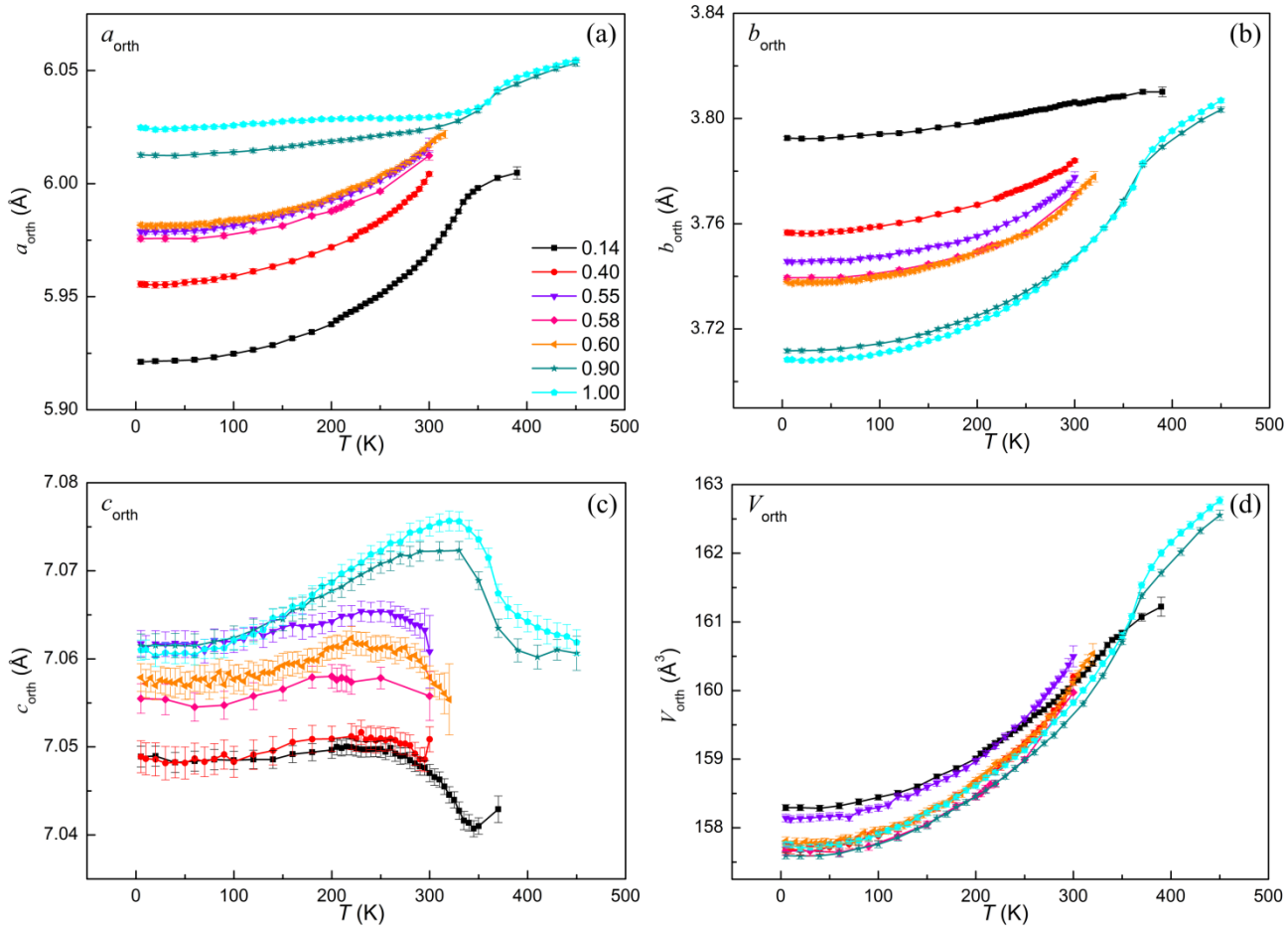

Figure S12 Thermal evolution of the lattice parameters in the orthorhombic structure of $Mn(Co_{1-x}Ni_x)Ge$ with x = 0.14, 0.40, 0.55, 0.58, 0.60, 0.90 and 1.00. The data comes from the refinement results of the neutron diffraction patterns.

5.2 Thermal evolution of Mn-Mn distances

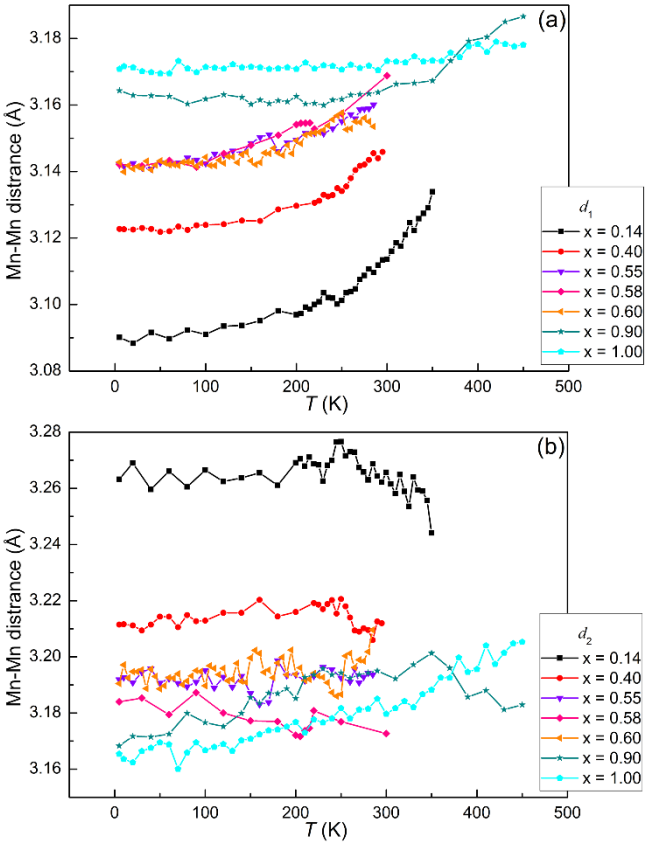

Figure S13 Thermal evolutions of the Mn-Mn distances, d_1 and d_2, in the orthorhombic structure of the $Mn(Co_{1-x}Ni_x)Ge$.

6 Magnetocaloric effect

As indicated by the phase diagram (Figure 9), inverse MCE and direct MCE are expected in the samples with x = 0.55 to 0.60. The magnetic isotherms with increasing field for $Mn(Co_{0.40}Ni_{0.60})Ge$ around T_N^{SP-FM} and T_M are shown in Figures. S14(a) and S14(b), respectively. In both figures, continuous metamagnetic behaviors are observed, confirming field-induced SP-AFM/FM and FM-Orth/PM-Hex transitions. It is also observed in Figure S14(a) that application of a field < 1 T is enough to align the spiral magnetic moments above 200 K, indicating the competition of the SP and FM structures.

Based on the isothermal magnetization measurement, the magnetic entropy changes $-\Delta S_M$ were calculated using Eq. 1 which derives by integrating the Maxwell function:[1]

$$\Delta S_M(T, \Delta H) = \mu_0 \int_{H_0}^{H_1} \left(\frac{\partial M(T, H')}{\partial T} \right)_H \mathrm{d}H'. \qquad (S-1)$$

Figure S14(c) is the contour image of the magnetic entropy change based on the magnetic isotherms in Figure S14(a). Positive magnetic entropy changes (inverse MCE, note: the calculation is based on magnetization measurement rather than demagnetization) are obtained, *e.g.* $-\Delta S_M^{peak}$ = -0.59(8) J kg^{-1} K^{-1} for $\mu_0\Delta H$ = 1 T at 197(2) K. Such positive magnetic entropy change results from the SP-AFM/FM transition, which occurs also in the samples with x = 0.55 and 0.58: $-\Delta S_M^{peak}$ ($\mu_0\Delta H$ = 1 T) = -0.48(7) J kg^{-1} K^{-1} and -0.52(8) J kg^{-1} K^{-1} at 142(4) K and 187(2) K, respectively. These values are comparable with the value of ~-0.75 J kg^{-1} K^{-1} ($\mu_0\Delta H$ = 1 T) in $Mn(Co_{0.38}Ni_{0.62})Ge$ reported by Zhang *et al*,[2] but smaller than -9.0 J kg^{-1} K^{-1} ($\mu_0\Delta H$ = 1 T) reported for $Mn(Co_{0.07}Ni_{0.93})Ge_{1.05}$.[3] In $Mn(Co_{0.07}Ni_{0.93})Ge_{1.05}$, the SP-AFM/FM transition is accompanied by a Orth/Hex structural transition, one kind of FOMST.[3] It is also noted that $-\Delta S_M^{peak}$ shifts quickly to low temperature with magnetic field as indicated by the dashed line in Figure S14(c), indicating strong dependence of the T_N^{SP-FM} on magnetic field.

In contrast to the case around T_N^{SP-FM} in Figure S14(c), negative magnetic entropy changes (direct MCE) are obtained due to field induced FM-Orth/PM-Hex transition around T_M as shown in Figure S14(d). The magnetic entropy changes maxima $-\Delta S_M^{peak}$ are 2.4(3) J kg^{-1} K^{-1} for $\mu_0\Delta H$ = 1 T and 14(2) J kg^{-1} K^{-1} for $\mu_0\Delta H$ = 5 T at 302(2) K. The former value is larger than counterpart (~1.6 J kg^{-1} K^{-1} for $\mu_0\Delta H$ = 1 T) in $Mn(Co_{0.38}Ni_{0.62})Ge$.[2]

In addition, the refrigeration capacity (*RC*) is also an important parameter for magnetocaloric materials, which is defined as:[4]

$$RC = \int_{T_{r1}}^{T_{r2}} |\Delta S_M| dT, \qquad (S-2)$$

T_{r1} and T_{r2} are the temperatures corresponding to the half-maximum of the isothermal magnetic entropy change peak $-\Delta S_{\mathrm{M}}^{\mathrm{peak}}$ and $T_{r1} < T_{r2}$. *RC*s in the present work are calculated using Eq. (S-2).

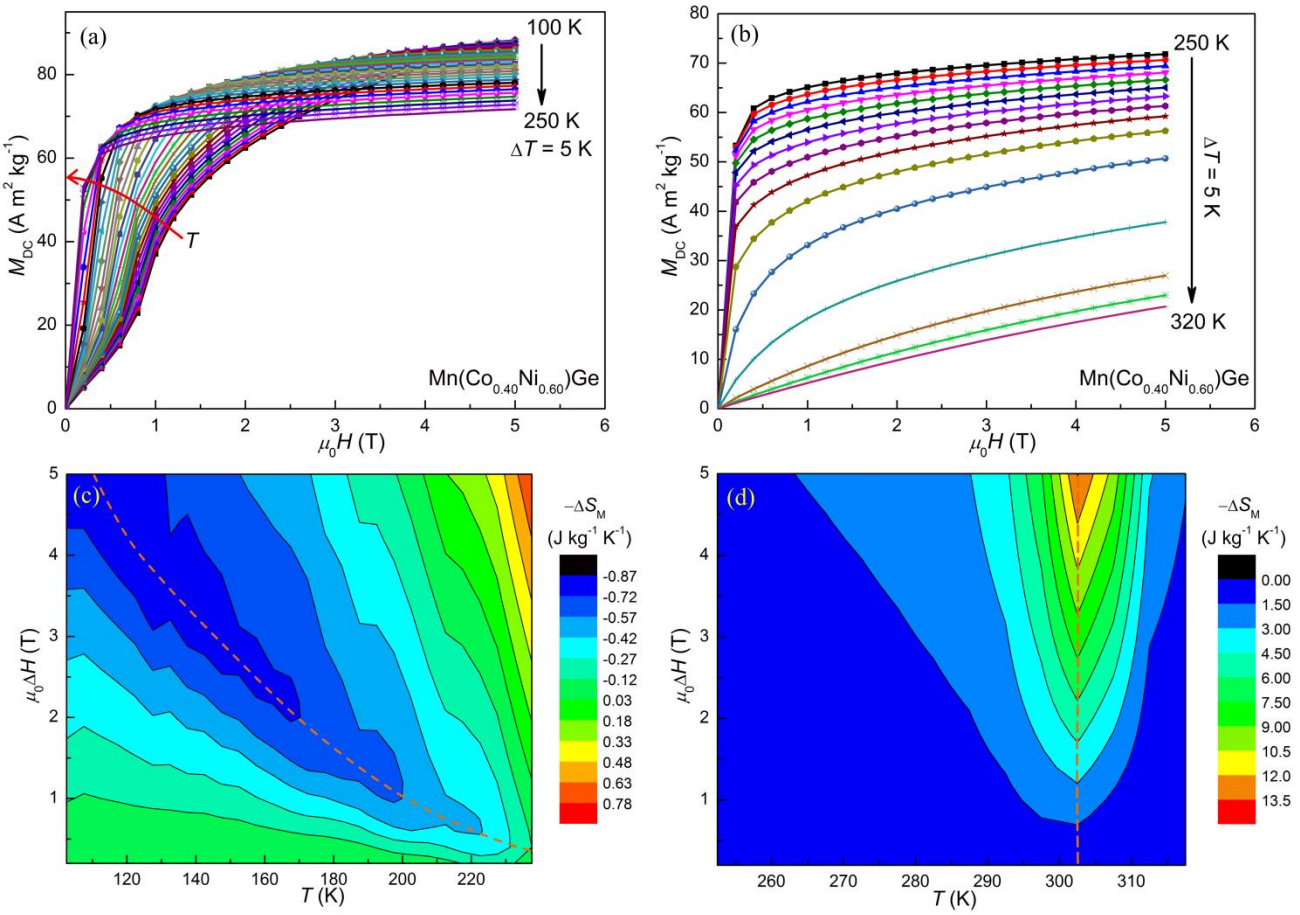

Figure S14 Isothermal magnetization of $Mn(Co_{0.40}Ni_{0.60})Ge$ around the transition temperatures (a) $T_{\mathrm{N}}^{\mathrm{SP-FM}}$ = 245(5) K and (b) T_{M} = 310(1) K. The measurement temperature increases (a) from 100 K to 250 K and (b) 250 K to 320 K with an interval of 5 K. (c) and (d) are the contour images of the isothermal magnetic entropy changes -ΔS_{M} with magnetic field changes from $\mu_0\Delta H$ = 0.2 T to $\mu_0\Delta H$ = 5.0 T around $T_{\mathrm{N}}^{\mathrm{SP-FM}}$ and T_{M}, respectively. The dashed line in (c) indicates that $T_{\mathrm{N}}^{\mathrm{SP-FM}}$ depends strongly on the magnetic field.

Table S4 Magnetic entropy changes ($-\Delta S_M$) and refrigeration capacities (*RC*) of the $Mn(Co_{1-x}Ni_x)Ge$ samples (x = 0.40, 0.50, 0.55, 0.58 and 0.60).

x	$\mu_0\Delta H$ (T)	$-\Delta S_M^{peak-1}$* (J kg^{-1} K^{-1})	T_{peak} (K)	$-\Delta S_M^{peak-2}$* (J kg^{-1} K^{-1})	T_{peak} (K)	$\mu_0\Delta H$ (T)	$-\Delta S_M^{peak-2}$* (J kg^{-1} K^{-1})	T_{peak} (K)	FWHM (K)	*RC* (J kg^{-1})
0.40	1	-	-	3.1(4)	292(2)	5	14(2)	292(2)	11(1)	140(20)
0.50	1	-	-	3.0(4)	284(2)	5	13(2)	284(2)	10(1)	120(20)
0.55	1	-0.48(7)	142(4)	3.3(4)	283(2)	5	15(2)	283(2)	10(1)	130(20)
0.58	1	-0.52(8)	187(2)	3.0(4)	285(2)	5	14(2)	285(2)	11(1)	140(20)
0.60	1	-0.59(8)	197(2)	2.4(3)	302(2)	5	14(2)	302(2)	11(2)	130(20)

* The two magnetic entropy changes, $-\Delta S_M^{peak-1}$ and $-\Delta S_M^{peak-2}$, corresponds to the SP-AFM/FM and FM-Orth /PM-Hex transitions around T_N^{SP-FM} and T_M, respectively. Inverse MCE and direct MCE are obtained around these two transitions.

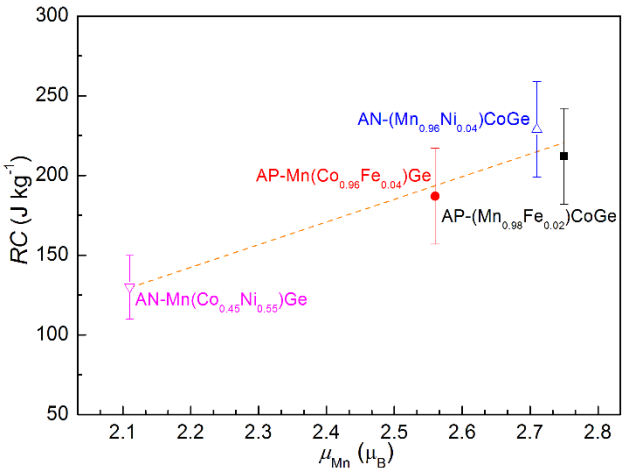

Figure S15 Relationship between *RC* and the magnetic moment of Mn sublattice at the temperature where the orthorhombic phase fraction is ~90 wt% for annealed $Mn(Co_{1-x}Ni_x)Ge$ (from this work), as-prepared $(Mn_{1-x}Fe_x)CoGe$ (x = 0.02),[5] as-prepared $Mn(Co_{1-x}Fe_x)Ge$ (x = 0.04)[6] and annealed $(Mn_{1-x}Ni_x)CoGe$ (x = 0.04).[7] The linear relationship between the *RC*s and the magnetic moments on Mn sublattice indicates that the smaller *RC*s in annealed $Mn(Co_{1-x}Ni_x)Ge$ is attributed to the relatively smaller magnetic moment in $Mn(Co_{1-x}Ni_x)Ge$.

References:

(1) Brück, E., Developments in magnetocaloric refrigeration. *J. Phys. D: Appl. Phys.* **2005,** 38, R381-R391.
(2) Zhang, C. L.; Chen, J.; Wang, T. Z.; Xie, G. X.; Zhu, C.; Wang, D. H., The magnetic phase transitions and magnetocaloric effect in $MnNi_{1-x}Co_xGe$ alloys. *Solid State Commun.* **2011,** 151, 1359-1362.
(3) Zhang, C.; Wang, D.; Cao, Q.; Ma, S.; Xuan, H.; Du, Y., The magnetostructural transformation and magnetocaloric effect in Co-doped $MnNiGe_{1.05}$ alloys. *J. Phys. D: Appl. Phys.* **2010,** 43, 205003.
(4) Gschneidner Jr, K. A.; Pecharsky, V. K.; Pecharsky, A. O.; Zimm, C. B., Recent Developments in Magnetic Refrigeration. *Materials Science Forum* **1999,** 315-317, 69-76.
(5) Ren, Q. Y.; Hutchison, W. D.; Wang, J. L.; Studer, A. J.; Din, M. F. M.; Pérez, S. M.; Cadogan, J. M.; Campbell, S. J., The magneto-structural transition in $Mn_{1-x}Fe_xCoGe$. *J. Phys. D: Appl. Phys.* **2016,** 49, 175003.
(6) Ren, Q. Y.; Hutchison, W. D.; Wang, J. L.; Studer, A. J.; Campbell, S. J., First-order magneto-structural transition and magnetocaloric effect in $Mn(Co_{0.96}Fe_{0.04})Ge$. *J. Alloys Compd.* **2017,** 693, 32-39.
(7) Ren, Q. New materials for magnetic refrigeration: the magnetocaloric effect in MnCoGe-based intermetallics. Doctoral thesis, The University of New South Wales, Canberra, Australia, 2016.